World Scientific
www.worldscientific.com

An approach to viscoelastic characterization of dispersive media by inversion of a general wave propagation model

Fernando Zvietcovich[*,‡], Jannick P. Rolland[†] and Kevin J. Parker[*]

[*]Department of Electrical and Computer Engineering
University of Rochester
Rochester, New York 14627, USA

[†]The Institute of Optics
University of Rochester
Rochester, New York 14627, USA
[‡]fzvietco@ur.rochester.edu

In the characterization of elastic properties of tissue using dynamic optical coherence elastography, shear/surface waves are propagated and tracked in order to estimate speed and Young's modulus. However, for dispersive tissues, the displacement pulse is highly damped and distorted during propagation, diminishing the effectiveness of peak tracking approaches, and leading to biased estimates of wave speed. Further, plane wave propagation is sometimes assumed, which contributes to estimation errors. Therefore, we invert a wave propagation model that incorporates propagation, decay, and distortion of pulses in a dispersive media in order to accurately estimate its elastic and viscous components. The model uses a general first-order approximation of dispersion, avoiding the use of any particular rheological model of tissue. Experiments are conducted in elastic and viscoelastic tissue-mimicking phantoms by producing a Gaussian push using acoustic radiation force excitation and measuring the wave propagation using a Fourier domain optical coherence tomography system. Results confirmed the effectiveness of the inversion method in estimating viscoelastic parameters in both the viscoelastic and elastic phantoms when compared to mechanical measurements. Finally, the viscoelastic characterization of a fresh porcine cornea was conducted. Preliminary results validate this approach when compared to other methods.

Keywords: Elastography; viscoelasticity; cylindrical waves; optical coherence tomography; shear waves; surface acoustic waves; viscoelastic phantoms.

[‡]Corresponding author.

F. Zvietcovich, J. P. Rolland & K. J. Parker

1. Introduction

Determining mechanical properties of tissue such as elasticity and viscosity is fundamental for better understanding and diagnosing pathological and physiological processes.[1,2] In this regard, optical coherence tomography-based elastography (OCE) offers the possibility of a noninvasive, high-resolution, and high-contrast measurement of tissue biomechanical properties.[3,4] For example, previous studies demonstrate the potential of OCE in assessing mechanical properties of different tissues such as cornea,[5,6] skin,[7] breast,[8] and liver.[9] In particular, a subset of dynamic OCE techniques uses short-duration pulses produced by a selected excitation source in order to produce mechanical wave propagation in the tissue being studied.[10] Excitation sources include acoustic radiation force (ARF), air-puff excitation, laser-based thermal expansion, and needles connected to piezoelectric vibrators, to name just a few.[11] By tracking the propagating wave, Young's modulus and other biomechanical parameters can be calculated based on the estimation of the wave speed and the selection of the correct wave propagation model dictated by the boundary conditions of the sample.[11]

Unfortunately, in many dispersive lossy tissues, propagation of shear or surface waves will be rapidly damped and distorted, complicating the attempts of estimating wave speed by using typical methodologies such as peak tracking.[12] Moreover, the estimation of viscous parameters in addition to the classic elastic modulus is of great interest since it can provide of useful information in the diagnosis of diseases such as the discrimination between malignant and benignant liver tumors[13] and the characterization of glioblastomas in human brain.[14] In optical coherence tomography (OCT), some work has been done for the viscoelastic measurement of tissue assuming a rheological model.[15–18] Most of them utilize frequency-dependent wave speed measurements to fit with theoretical models of dispersion (rheological models), disregarding valuable information given by the wave attenuation process. Therefore, the use of model-independent approaches for the viscoelastic characterization of tissue is an important trending topic in elastography since it can provide an accurate intrinsic information without assumptions of the tissue mechanical behavior, which is in many cases unknown.

Few model-independent approaches have been proposed in ultrasound elastography,[12,19–22] and in OCE.[23] In ultrasound, Schmitt *et al.*[19] proposed a method for the calculation of the complex shear modulus by the estimation of shear wave dispersion and attenuation of a sinusoidal continuous plane wave. Nenadic *et al.*[20] proposed a 2D Fourier approach for the analysis of a cylindrically spreading continuous waves and the estimation of speed dispersion and attenuation. Kazemirad *et al.*[21] estimated the complex shear modulus by fitting an analytical model of a continuous cylindrical shear wave with a shear pulse generated using ARF excitation. In OCE, Leartprapun *et al.*[23] proposed a model-independent method for the reconstruction of complex shear modulus from measurements of continuous hemi-spherical surface waves produce by ARF excitation in viscoelastic media. While these approaches calculate viscoelastic properties of tissue without using a rheological model, some assumptions made may produce biased results. For instance, in Ref. 19, the plane wave assumption can be difficult to satisfy for most of the excitation methods. Also, Refs. 20, 21, and 23, assume that waves will be observed in the asymptotic range far from the excitation source which may not be possible if the wave is highly attenuated by dispersive lossy media. Finally, Parker and Baddour[12] investigated the propagation of a cylindrical axisymmetric Gaussian shear wave in a viscoelastic media by proposing a full analytical model-independent solution that takes a first-order approach to dispersion.

In this paper, we invert a general wave propagation model following the approach of Parker and Baddour[12] that incorporates space-time propagation, decay, and distortion of pulses in a dispersive medium in order to accurately estimate the elastic and viscous components of such a medium. The model contemplates the initial shape of ARF push in space and time and uses a general first-order approximation of dispersion, avoiding the use of any particular rheological model of tissue. Experiments will be conducted in elastic and viscoelastic tissue-mimicking phantoms by producing a Gaussian push using ARF excitation, and measuring the surface wave propagation using a Fourier domain optical coherence tomography (FD-OCT) system. Results found in the inversion method will be compared to mechanical measurements (MM) for validation. Finally, we will conduct a preliminary experiment in a fresh porcine cornea in order confirm the validity of our approach in real viscoelastic tissue.

2. Theory

2.1. *Shear wave pulse in an infinite media*

An ultrasound (US)-based ARF excitation beam with a Gaussian intensity axisymmetric profile in cylindrical coordinates (r, θ, z) is given by

$$I(r, \theta, z) = \left(\frac{1}{2\sigma^2}\right) e^{-r^2/4\sigma^2} \qquad (1)$$

in the r-direction, and extending uniformly in the axial (z) direction, where $\sigma^2 = $ half variance of the pulse, $r = (x^2 + y^2)^{1/2}$, $\theta = \text{atan}(y/x)$ as shown in Fig. 1. Particle velocity and displacement are set to be zero everywhere as initial conditions in an infinite and homogeneous dispersive medium. We assume that, given the ARF direction and extent, the displacements are polarized in the z-direction, and the derivatives with respect to θ and z are zero. Then, Eq. (1) can be written as $I(r)$, and using the notation of Graff,[24] we can define the governing equation in a viscoelastic medium as

$$\nabla^2 u_z(r, t) - \frac{1}{c^2}\frac{\partial^2 u_z(r, t)}{\partial t^2} = -F_z(r)T(t), \qquad (2)$$

where u_z is the displacement of the shear wave in the z-direction; c is the velocity of the shear wave; $F_z(r)$ is the applied body force proportional to
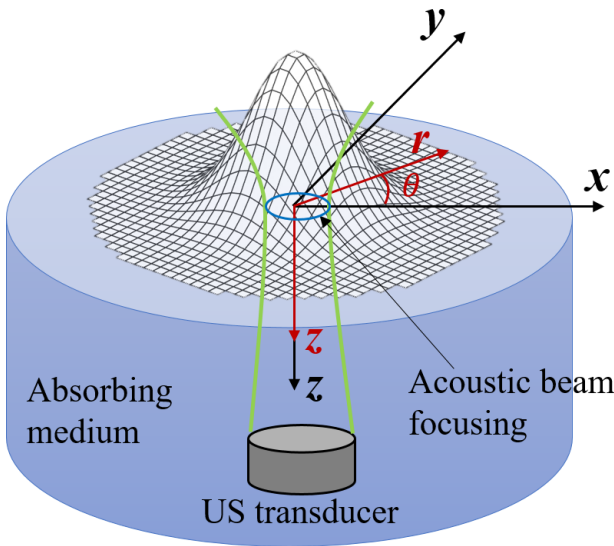

Fig. 1. Schematic of a Gaussian-shaped pulse produced in a dispersive medium by an ultrasound ARF transducer. The center of the pulse is the origin for the Cartesian and cylindrical coordinate system.

the ARF beam $I(r)$; and $T(t)$ is the temporal application, which we will take as a rectangular function of duration a delayed $a/2$, $\text{rect}(\frac{t}{a} - \frac{1}{2})$.

The Laplacian operator in cylindrical coordinates reduces to $\nabla^2 = \frac{\partial^2}{\partial r^2} + \frac{1}{r}\frac{\partial}{\partial r}$. Applying the Hankel transform $\mathbf{H}$ in the space, and the nonunitary angular frequency Fourier transform $\mathfrak{J}$ in time to Eq. (2) in cylindrical coordinates yields

$$-\varepsilon^2 \hat{U}(\varepsilon, \omega) + \frac{\omega^2}{c^2}\hat{U}(\varepsilon, \omega) = -\hat{F}(\varepsilon)\hat{T}(\omega), \qquad (3)$$

where $\hat{U}(\varepsilon, \omega) = \mathfrak{J}\{\mathbf{H}\{u_z(r, t)\}(\varepsilon, t)\}(\varepsilon, \omega)$, ε is the spatial frequency, ω is the temporal frequency, $\hat{F}(\varepsilon) = \mathbf{H}\{F_z(r)\}(\varepsilon)$, and $\hat{T}(\omega) = \mathfrak{J}\{T(t)\}(\omega)$. Then, Eq. (3) can be written as

$$\hat{U}(\varepsilon, \omega) = \frac{\hat{F}(\varepsilon)\hat{T}(\omega)}{\varepsilon^2 - k^2}, \qquad (4)$$

where k is the wavenumber. In a dispersive medium, the wavenumber is treated as a complex number $k = \frac{\omega}{c} - i\alpha$, where α is the absorption coefficient. Then, we apply the inverse Hankel transform to Eq. (4) as follows

$$\hat{u}(r, \omega) = \int_0^\infty \frac{\hat{F}(\varepsilon)\hat{T}(\omega)}{\varepsilon^2 - k^2} J_0(\varepsilon r)\varepsilon d\varepsilon. \qquad (5)$$

where J_0 is the Bessel function of the first kind. Then, by applying Baddour's theorem[25] and selecting the appropriate solution according to the Sommerfield radiation condition we obtain

$$\hat{u}(r, \omega) = -\frac{\pi i}{2}H_0^{(2)}(kr)\hat{F}(k)\hat{T}(\omega), \qquad (6)$$

where $H_0^{(2)}(x)$ is a Hankel function of the second kind. The form of Eq. (6) when the temporal application of the force $F_z(r)$ is instantaneous $(T(t) = \delta(t))$ can be found in Parker and Baddour.[12] Here, we seek a form when the force $F_z(r)$ with a Gaussian beam pattern (Eq. (1)) is applied for a transient time a in the media. Let

$$F_z(r)T(t)$$

$$= \left[A_0\left(\frac{1}{2\sigma^2}\right)e^{-r^2/4\sigma^2}\right]\left[\text{rect}\left(\frac{t}{a} - \frac{1}{2}\right)\right], \qquad (7)$$

where A_0 is the force amplitude, and σ is related to the curve width. Then, applying the spatial Hankel and temporal Fourier transforms to Eq. (7), we

have

$$\hat{F}(k)\hat{T}(\omega) = [A_0 e^{-\sigma^2 k^2}]\left[e^{-\frac{i\omega a}{2}}\mathrm{sinc}\left(\frac{\omega a}{2\pi}\right)\right], \qquad (8)$$

where $\mathrm{sinc}(x) = \frac{\sin(\pi x)}{\pi x}$. We are interested in finding the analytic solution of Eq. (6) for particle velocity $\hat{v}(r,\omega) = i\omega \hat{u}(r,\omega)$. Then, using Eqs. (6) and (8), we have

$$\hat{v}(r,\omega) = A_0 \frac{\pi\omega}{2} H_0^{(2)}(kr) e^{-\sigma^2 k^2} e^{-\frac{i\omega a}{2}}\mathrm{sinc}\left(\frac{\omega a}{2\pi}\right), \quad (9)$$

which is a closed-form analytical solution in the $r - \omega$ space that describes the cylindrical spreading of the pulsed wave, attenuation, and dispersion when it propagates through a viscoelastic medium.

2.2. Viscoelastic modeling of the medium

As discussed by Carstensen,[26] a variety of loss mechanisms with their own frequency-dependent solutions exist in viscoelastic materials, such as Kelvin–Voigt, Kelvin–Voigt fractional derivative, standard linear solid, and relaxation and hysteresis models. Given the uncertainties in appropriate choice of rheological model, we seek a general solution that is mechanism-independent. Therefore, we solely assume a limited shear wave frequency bandwidth of the excitation in which a Taylor series expansion can be used to express the frequency-dependent behavior of the medium. Then, we introduce a first-order Taylor approximation of the frequency-dependent phase speed c and attenuation α of the wave such that

$$c \equiv c_0 + c_1 \cdot |\omega| \quad \text{and} \quad \alpha \equiv \alpha_0 + \alpha_1 \cdot |\omega|, \quad (10)$$

where $c_0 \gg c_1\omega$. As described by the most conventional loss mechanisms,[27] as $\omega \to 0$, $c \to c_0$ and $\alpha \to 0$. Then, we can consider $\alpha_0 = 0$ for a conventional dispersive medium. Therefore, the complex frequency-dependent wavenumber will be described as

$$k(\omega) = \frac{\omega}{c_0 + c_1|\omega|} - i\alpha_1|\omega|, \qquad (11)$$

and this form is used in Eq. (9) for k. For further notation simplification, we call $k'(\omega) = \frac{\omega}{c_0 + c_1|\omega|}$, and $k''(\omega) = \alpha_1|\omega|$. In a linear and isotropic viscoelastic material, the complex shear modulus $G^*(\omega) = G'(\omega) + iG''(\omega)$, where $G'(\omega)$ is the shear storage,

and $G''(\omega)$ is the loss moduli, can be obtained using the real and imaginary parts of the wavenumber in Eq. (11)[21] as

$$G'(\omega) = \rho\omega^2 \frac{k'(\omega)^2 - k''(\omega)^2}{(k'(\omega)^2 + k''(\omega)^2)^2}, \qquad (12a)$$

$$G''(\omega) = 2\rho\omega^2 \frac{k'(\omega)k''(\omega)}{(k'(\omega)^2 + k''(\omega)^2)^2}, \qquad (12b)$$

where ρ is the density of the material. In Figs. 2(a) and 2(c), the magnitude of Eq. (9) is plotted in the $r - \omega$ space for the viscoelastic ($c_0 \neq 0, c_1 \neq 0$, $\alpha_1 \neq 0$), and pure elastic ($c_0 \neq 0, c_1 = 0, \alpha_1 = 0$) cases, respectively. Estimates in $r = 0$ were disregarded since $H_0^{(2)}(kr)$ has a singularity at the origin. Moreover, particle velocity profiles versus r-axis, $\hat{v}(r, t_0) = \mathfrak{J}^{-1}\{\hat{v}(r,\omega)\}(t_0)$, at different instants t_0 for both cases are shown in Figs. 2(b) and 2(d). In the pure elastic case, the rapid decease in amplitude follows the asymptotic cylindrical spreading $1/\sqrt{kr}$; while in the viscoelastic case, the low-pass smoothing of the particle velocity waveforms is evident, which diminishes the effectiveness of peak tracking approaches.

2.3. Shear to surface acoustic wave relationship

Surface acoustic waves (SAW) are produced when a vibration is generated at a solid–vacuum or solid–fluid interface.[28,29] This work is intended for optical coherence elastography (OCE) applications. Therefore, we use an OCT system to acquire motion frames. Since the penetration depth of this system is typically some millimeters from the interface, SAW are more likely to be scanned than shear waves. If we consider a semi-infinite solid medium, the predominant SAW propagating in the solid-vacuum interface are Rayleigh waves.[28] The relationship between shear wave and Rayleigh wave phase speed in a linear isotropic medium for a Poisson's ratio $\nu \approx 0.5$ is given by[29]

$$c \approx 1.05 * c_{\mathrm{Rayleigh}}. \qquad (13)$$

Moreover, Rayleigh waves from a point source follow cylindrical spreading $1/\sqrt{kr}$ as described in Ref. 29, which is consistent with the asymptotic form of the Hankel term in Eq. (9), $|H_0^{(2)}(kr)| \cong \sqrt{\frac{2}{\pi kr}}$, for complex values of k.[30] Therefore, making
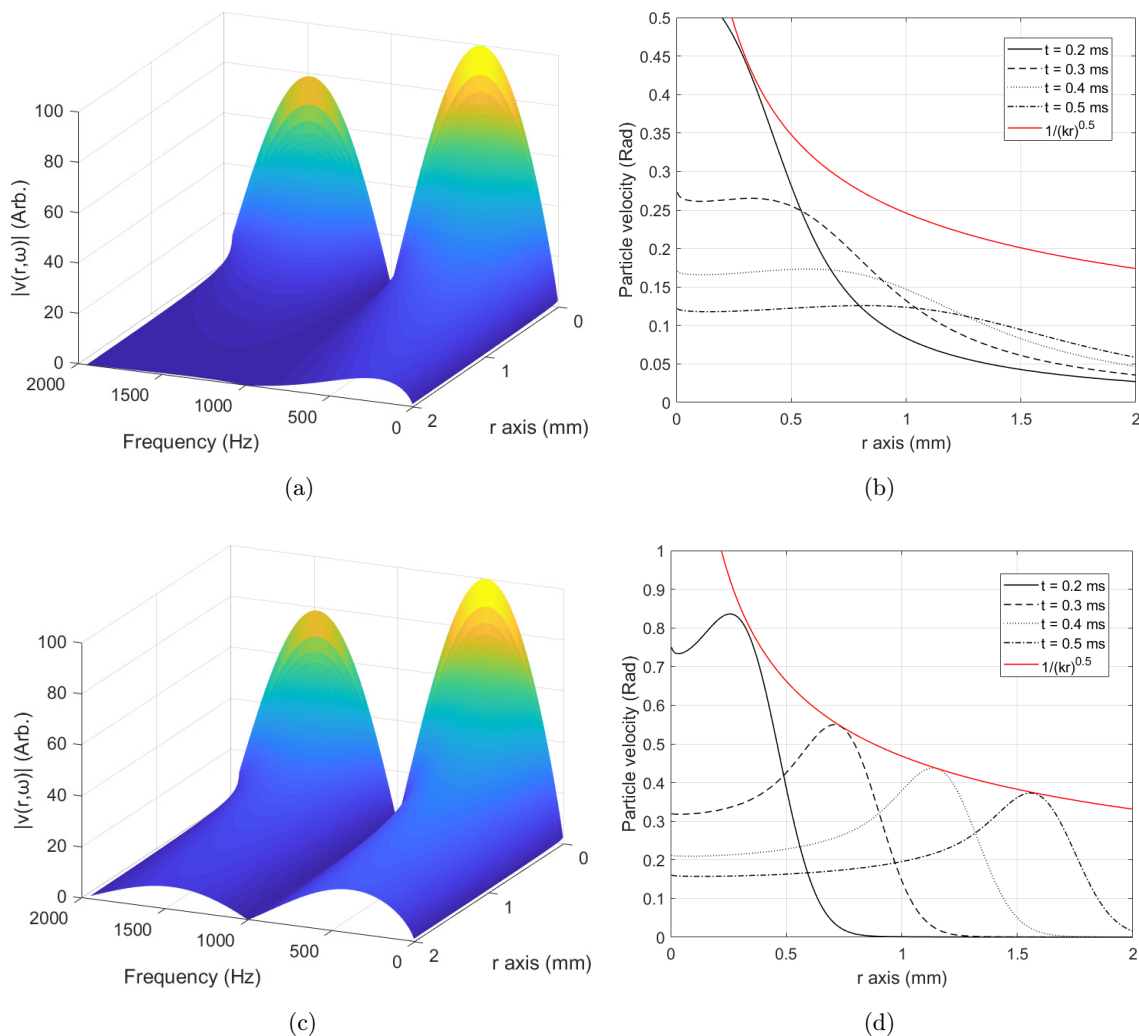
(a)

(b)

(c)

(d)

Fig. 2. Theoretical plots $|\hat{v}(r,\omega)|$ (left col.) and $\hat{v}(r,t_0) = \mathfrak{J}^{-1}\{\hat{v}(r,\omega)\}(t_0)$ (right col.) for a viscoelastic (a,b) and elastic (c,d) media. $\omega = 2\pi f$, and f = frequency. For all cases, the input force is a Gaussian pulse as described in Eq. (7), with $\sigma = 0.1$ mm, and $a = 1$ ms. The material properties are selected as $c_0 = 4$ m/s, and $c_1 = 1 * 10^{-11} \frac{m}{s}$/Hz. $\alpha_1 = 0.15 \frac{Np}{m}$/Hz, and $\alpha_1 = 0.0015 \frac{Np}{m}$/Hz for the viscoelastic and elastic cases, respectively. Particle velocity units are shown in radians referring to OCT Doppler phase-shift and can be transformed to m/s using Eq. (16).

the adjustment for phase speed as described in Eq. (13), the shear wave model of Eq. (9) is suitable for describing the Rayleigh wave propagation at a given depth z_0.

3. Materials and Methods

3.1. *Sample preparation and measurement*

Two tissue-mimicking phantoms where used in experiments. A cylindrically-shaped custom shear wave viscoelastic phantom (model No. 16410001, CIRS, Virginia, USA) was used as the dispersive medium (5.4 cm in diameter × 2.2 cm in height).

A cylindrically-shaped aqueous elastic phantom (Aquaflex US del pad, Parker Laboratories INC., New Jersey, USA) was selected as the elastic medium (9 cm in diameter × 2 cm in height). The frequency-dependent Young's modulus of each phantom was measured using a stress–relaxation by compression test. The measurement was conducted using a MTS Q-Test/5 Universal Testing Machine (MTS, Eden Prairie, Minnesota, USA) with a 5 N load cell using a compression rate of 0.5 mm/s, a strain value of 5%, and total measurement time of 600 s. The stress-time plots obtained by the machine were fitted to a three-parameter Kelvin–Voigt fractional derivative (KVFD) model[31] for the calculation of frequency-dependent complex Young's
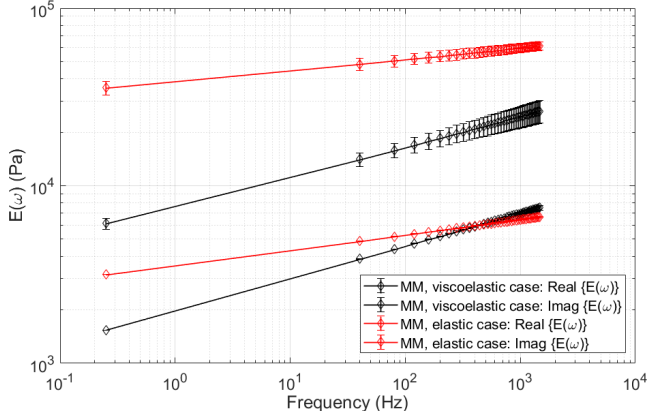
Fig. 3. Log–log of frequency-dependent complex Young's modulus for the elastic and viscoelastic phantoms obtained from mechanical measurements (MM) using a stress relaxation by compression test. $\omega = 2\pi f$, and f = frequency. Frequency-dependent results are predictions of the Kelvin–Voigt fractional derivative model and do not represent independent measurements over the frequency range.

modulus given as

$$E^*(\omega) = \left[E_0 + \eta \cos\left(\frac{\pi\tau}{2}\right)\omega^\tau\right] + i\left[\eta \sin\left(\frac{\pi\tau}{2}\right)\omega^\tau\right], \quad (14)$$

where E_0 is the relaxed elastic constant, η is the viscous parameter, and τ is the order of fractional derivative. Measurements were conducted in three samples of each phantom type in order to calculate the mean and standard deviation (error) for each predicted frequency-dependent result. Figure 3 shows the real and imaginary parts of Eq. (14) versus frequency for both phantoms. Then, for a nearly incompressible (Poisson's ratio close to 0.5), homogeneous, and isotropic medium, the complex phase velocity of the shear wave for each phantom with a material density of ρ can be calculated[1] as $c^* = \sqrt{G^*/\rho} = \sqrt{E^*/(3\rho)}$, and the complex

wavenumber of Eq. (11) can be expressed as

$$k(\omega) = \frac{\omega}{c^*} = \left[\frac{\omega}{\sqrt{2/(3\rho)}} \frac{\sqrt{|E^*| + E'}}{|E^*|}\right] - i\left[\frac{\omega}{\sqrt{2/(3\rho)}} \frac{\sqrt{|E^*| - E'}}{|E^*|}\right], \quad (15)$$

where $E' = \text{Real}\{E^*\}$. For both phantoms, $\rho = 1\,\text{g/cm}^3$. The three estimated parameters of the KVFD model are detailed in Table 1. We also included results of a compression test on the same phantoms in order to estimate the quasi-static Young's modulus $E(\omega \approx 0)$, and the equivalent shear wave speed $c(\omega \approx 0)$. The equivalent frequency for the quasi-static compression test rate was found to be 0.25 Hz which is very low compared to the peak frequency band of the ARF shear waves. Predictions of the real part of the Young's modulus given by the KVFD model at $f \approx 0.25$ Hz (first frequency sample in Fig. 3) are similar to results found in the quasi-static compression test which partially supports the validity of the model.

Mechanical testing results in phantoms are fundamental for the validation of our proposed approach. Therefore, the selection of the correct rheological model which describes the relationship between the frequency-dependent prediction and the stress–relaxation test is required. Both elastic and viscoelastic phantoms were well-characterized using the KVFD model since a higher r-square fitting quality (0.999) was found as compared to other rheological models: Voigt, Kelvin–Voigt, Zener, Standard Linear Solid, and Standard Linear Solid Fractional Derivative models.

For the biological tissue test, we selected a porcine cornea. A fresh porcine eyeball was obtained from an abattoir (Joe's Meat Market, Ontario, NY, USA) with all experiments being performed within 12 h of their collection. For the scanning of the

Table 1. Mechanical testing results in elastic and viscoelastic phantoms. Kelvin–Voigt fractional derivative parameters (left col.) and compression test results (right col.) are shown for both media. Quasi-static shear wave speed was calculated using $c(\omega \approx 0) = \text{Real}\{\sqrt{E^*/(3\rho)}\}$ for $\rho = 1\,\text{g/cm}^3$ and assuming incompressibility. All experiments were performed at room temperature (25°C).

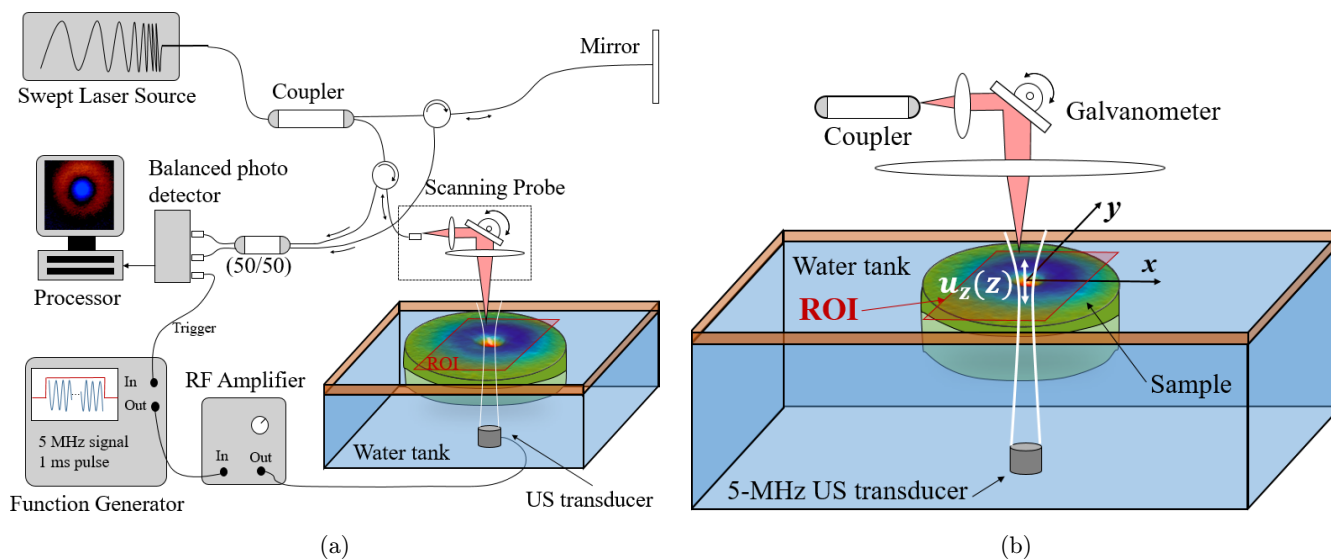|	Stress relaxation test: Kelvin–Voigt fractional derivate model parameters			Quasi-static compression test: Young's modulus and shear speed	
	E_0 (kPa)	η (kPa s^α)	τ	$E(\omega \approx 0)$	$c(\omega \approx 0)$
Viscoelastic phantom	0.711 ± 0.481	5.203 ± 0.852	0.178 ± 0.028	4.98 ± 0.24	1.29 ± 0.02
Elastic phantom	9.969 ± 9.661	24.928 ± 12.217	0.086 ± 0.025	34.51 ± 0.85	3.39 ± 0.04

Fig. 4. Experimental setup. (a) PhS-OCT system implemented with a swept-source laser for motion detection. (b) Placement of the sample in a water tank, ARF US-transducer, and region of interest (ROI). Motion is produced in the surface of the sample.

cornea, the eyeball was immersed in a tank with saline solution at $25°C$ leaving the corneal tissue in contact with the air. The intra-ocular pressure (IOP) of the eyeball was measured during the experiment using a digital pressure gage (model DPGWB-04, Dwyer Instruments Inc., Michigan City, Indiana, USA). The average IOP reported during experiments was 9.3 mmHg.

3.2. *Experimental setup*

The experimental setup is shown in Fig. 4(a). A 5 MHz confocal ultrasonic transducer (PIM7550-2inchFL, Dakota Ultrasonics, California, USA) with 5.01 cm of focal length was excited with a 1 ms sinusoidal tone of 5 MHz provided by a function generator (AFG320, Tektronix, USA). The generator was connected to a RF power amplifier (25A250, Amplifier Research, Souderton, PA, USA) in order to produce an approximate Gaussian, radially symmetric ($\sigma = 0.338$ mm) focused ARF push within the sample at the air–solid surface interface of the sample. The ultrasonic transducer was coupled to the sample with saline water as shown in Fig. 4(b). A phase-sensitive optical coherence tomography (PhS-OCT) system implemented with a swept source laser (HSL-2100-WR, Santec, Aichi, Japan) of a center wavelength of 1318 nm was used to acquire 3D motion frames of the sample within a region of interest (ROI) of 10×10 mm in the xy-plane, and a maximum depth of 2.5 mm in the

z-plane. The OCT acquisition and the excitation of the 5 MHz transducer were triggered by the computer controlling the entire process.

The ARF push was focused at a certain (x_0, y_0) position in the sample's surface [Fig. 4(b)], and it produced a localized out-of-plane vertical displacement which generated a cylindrically-shaped Rayleigh wave propagating within the ROI. The ARF vibration amplitude in the sample was adjusted to less than the maximum displacement ($u_{z,\max}$) that can be detected by the OCT system without unwrapping the Doppler phase signal. For all cases, we used Eq. (12) to convert Rayleigh wave speed to shear wave speed.

The PhS-OCT characteristics include a full-width half-maximum (FWHM) bandwidth of 125 nm, and a light source frequency sweep rate of 20 kHz. The source power that entered the OCT interferometer was split by a 10/90 fiber coupler into the reference and sample arms, respectively. In the reference arm, a custom Fourier domain optical delay line was used for dispersion compensation. In the sample arm, a collimated light beam diameter of 6.7 mm at $1/e^2$ was directed onto a test phantom by a focusing imaging lens (LSM05, Thorlabs Inc., NJ, USA), coupled with a galvanometer scanning mirror placed at the front focal plane of the imaging lens to achieve telecentric scanning. The back-scattered light from the sample was recombined with the light reflected from the reference mirror with a 50/50 fiber coupler. The time-encoded spectral interference signal was

F. Zvietcovich, J. P. Rolland & K. J. Parker

detected by a balanced photo-detector (1817-FC, New Focus, CA, USA), and then digitized with a 500 Msamples/s, 12-bit-resolution analog-to-digital converter (ATS9350, AlazarTech, QC, CA). The maximum sensitivity of the system was measured to be 112 dB.[32] The imaging depth of the system was measured to be 5 mm in air (-10 dB sensitive fall-off). The optical lateral resolution was approximately $30\,\mu$m, and the FWHM of the axial point spread function after dispersion compensation was $10\,\mu$m. The synchronized control of the galvanometer and the OCT data acquisition was conducted through a LabVIEW platform (National Instruments, Austin, TX, USA) connected to a workstation. The phase stability of the system was calculated as the standard deviation of the temporal fluctuations of the Doppler phase-shift ($\Delta\phi_{\mathrm{err}}$) while imaging a static structure.[33] Results show $\Delta\phi_{\mathrm{err}} = 4.6$ mrad when using Loupas' algorithm.[34] The displacement sensitivity is measured as the minimum detectable axial particle displacement ($u_{z,\mathrm{min}}$). We found $u_{z,\mathrm{min}} = 0.358$ nm. Finally, the maximum axial displacement supported by the system without unwrapping the phase-shift signal ($\Delta\phi_{\mathrm{max}} = \pi$) is $u_{z,\mathrm{max}} = 0.24\,\mu$m.

3.3. Acquisition and processing approach

Due to speed limitations of the OCT acquisition system, a complete phase front of a single ARF excitation cannot be instantly acquired within a ROI. Therefore, a repeated excitation/acquisition triggered at any single spatial location within the ROI is conducted. This method is also called the M-B mode acquisition protocol, as described in Ref. 10. Methodologically, in a medium with refractive index n, the phase difference $\Delta\phi(z) = \phi(z, t_1) - \phi(z, t_0)$ at

two consecutive instants t_0 and t_1 ($t_0 < t_1$), for a given (x_o, y_o) position, is related to the particle velocity in the axial direction by

$$v_z(z) = \Delta\phi(z)\frac{\lambda_0}{4\pi n \Delta_M}, \qquad (16)$$

where ϕ is the phase of the A-line signal acquired with the OCT system, n is the refractive index of the medium, λ_0 is the center wavelength of the laser, and Δ_M is the time sampling resolution. We select the Loupas' algorithm[34] for the accurate estimation of $\Delta\phi(z)$ which increased the signal-to-noise ratio compared to other approaches as demonstrated by Zvietcovich *et al.*[10]

The repeated acquisition and ARF excitation is possible since they are synchronized with the same cyclic trigger signal of 7 ms periodicity. The ARF tone is formed by 5000 cycles of a 5-MHz harmonic wave equivalent to 1 ms excitation. The M-B mode approach is used for generating x-axis space-time representations of particle velocity $v_z(z)$ at a given z_0 and y_0 position. In this study, we constrained the analysis to the surface of the sample so that z_0 corresponds to the axial position of surface for any (x_0, y_0) location. Each M-B acquisition spans 200 locations in the x-axis (10 mm), and $M = 100$ time samples (5 ms) as shown in Fig. 5. Then, we repeat this process at each location y_0 in the y-axis for 200 positions (10 mm).

In total, we acquired a 3D matrix volume of $200 \times 200 \times 100$ measurements of $v_z(z_0)$ in the x, y, and time axes, respectively, using the described protocol in order to cover the ROI of 10×10 mm at z_0, and 5 ms in the time frame. Each profile cut of the 3D matrix in the xy-plane corresponds to a motion frame at a frame rate of 20 kHz (time resolution $\Delta_M = 50\,\mu$s). The total acquisition time was 4.6 min.
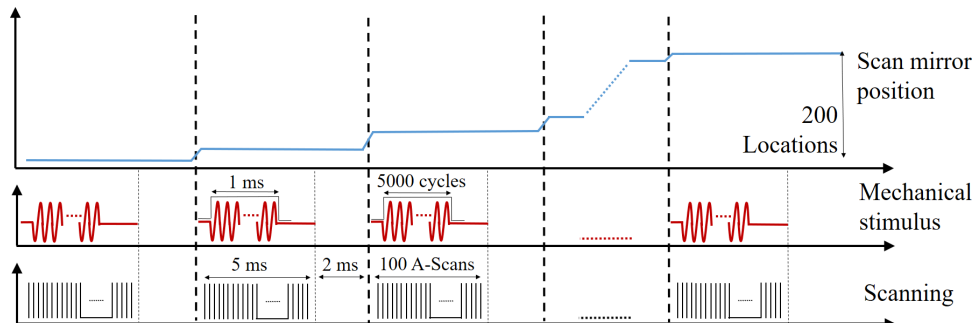

Fig. 5.   M-B mode for acquisition protocol of motion signals using a PhS-OCT system.

3.4. *Inversion approach*

In Sec. 3.3, a 3D matrix representing particle velocity at the surface of the sample was acquired using the OCT system. Without loss of generality, we can call that data matrix $v_{z_0}(x,y,t)$, where x and y represent spatial coordinates on the surface, and t is the time domain. We want to fit the analytical model of Eq. (9) — $\hat{v}(r,\omega)$ — to the data in $v_{z_0}(x,y,t)$, however, $\hat{v}(r,\omega)$ is defined in the cylindrical r-axis. Therefore, taking a profile cut of $v_{z_0}(x,y,t)$ along the xy-plane containing the center of the ARF excitation, and cropping the data to achieve a one-sided propagation matrix, we obtain $v_{z_0}(r,t)$.

Taking $\hat{v}_{z_0}(r,\omega) = \mathfrak{J}\{v_{z_0}(r,t)\}$, and deriving A_0 in Eq. (9) by normalizing the data with the model for the maximum peak value, we can solve

$$\{c_0^*, c_1^*, \alpha_1^*\} = \operatorname*{arcmin}_{c_0, c_1, \alpha_1} \||\hat{v}(r,\omega)| - |\hat{v}_{z_0}(r,\omega)|\|_2^2 \tag{17}$$

for the unknown parameters c_0, c_1, and α_1. Equation (17) is a nonlinear least squares problem and we employ the Levenberg–Marquardt method[35] for generating a solution. We solved Eq. (17) in four profile cuts of $v_{z_0}(x,y,t)$ at angles $[0; \pi/4; \pi/2; 3\pi/4]$ rad for the posterior calculation of average and standard deviation (error) of the estimated predictions.

4. Results and Discussion

4.1. *Phantom experiments*

Figure 6 shows particle velocity frames $v_{z_0}(x,y;\{t_0, t_1, t_2\})$ for three different time instants extracted at the surface of each phantom as described in Sec. 3.3. We defined the initial time $t=0\,s$ at the falling edge of the ARF pulse. The ARF push location is found to be approximately at the center of the ROI. The cylindrical spreading of the wave when traveling out of the source is evident in both cases as shown in Fig. 6(e). The attenuation of the peak is more pronounced in the viscoelastic case when compared to the elastic case, as expected.

Profile cuts in the x-direction centered to contain the ARF excitation origin were obtained from $v_{z_0}(x,y,t)$ in the viscoelastic and elastic cases as shown in Figs. 7(a) and 7(b), respectively. A Gaussian bell shape is initially observed at the first instant as described in Sec. 2.1. We fit $F_z(r)$ from Eq. (7) to this curve in order to estimate σ, which is necessary for solving Eq. (17). Results are shown in Table 2. In addition, parameter a in the rectangular function of Eq. (7) is set to be $a = 1\,ms$ as described in Sec. 3.3. Figures 7(c) and 7(d) show $|\hat{v}_{z_0}(r,\omega)|$ plots for the viscoelastic and elastic cases, respectively. The appearance of the sinc function in the frequency axis confirms the validity of $\hat{T}(\omega)$ in Eq. (8). Moreover, the attenuation of the main lobe in $|\hat{v}_{z_0}(r,\omega)|$ for the viscoelastic case tends to move
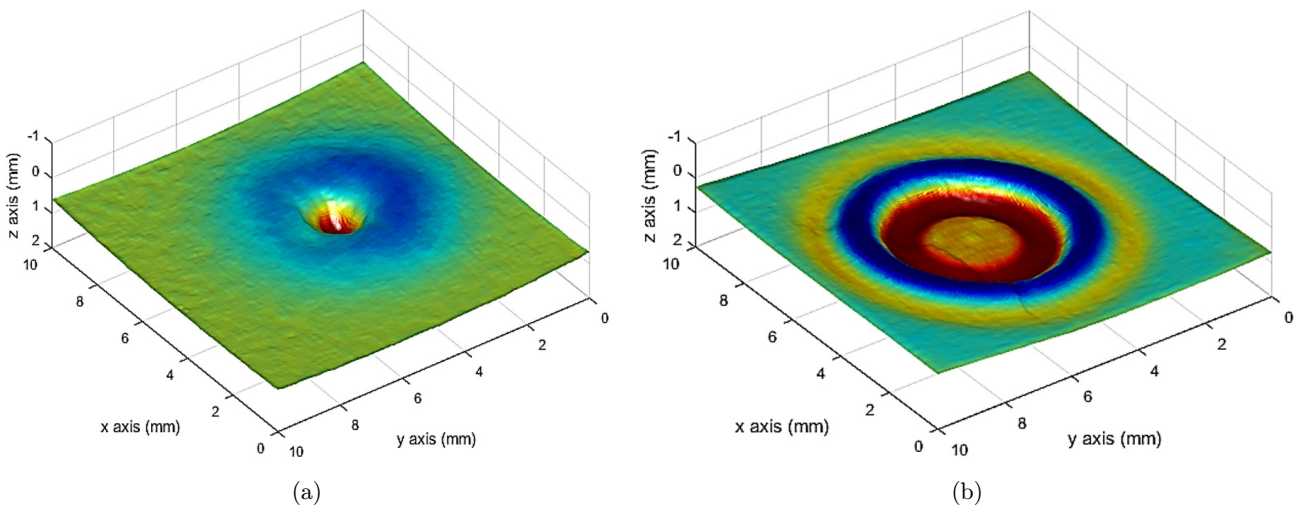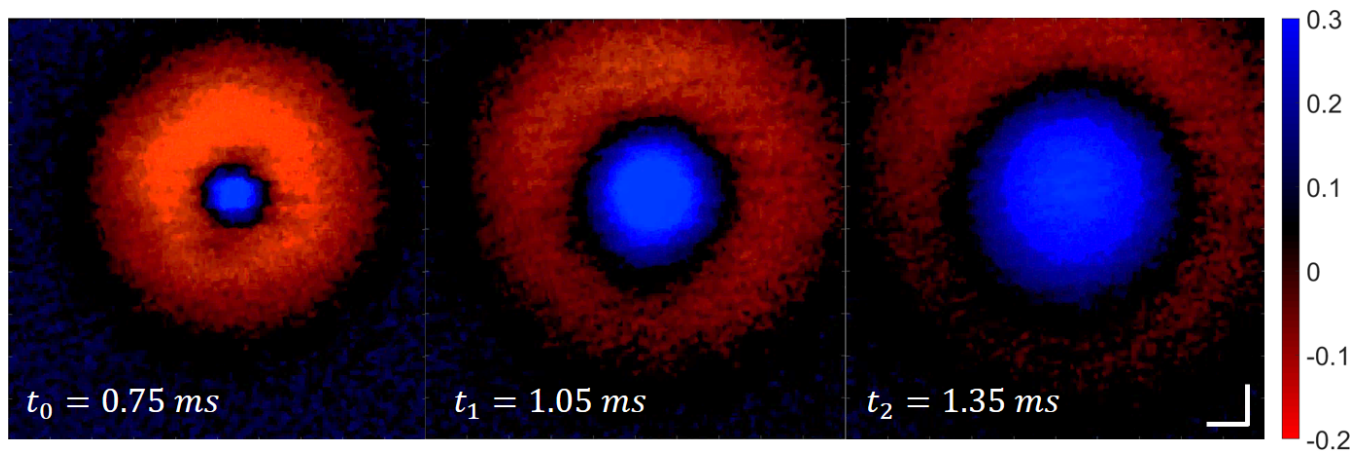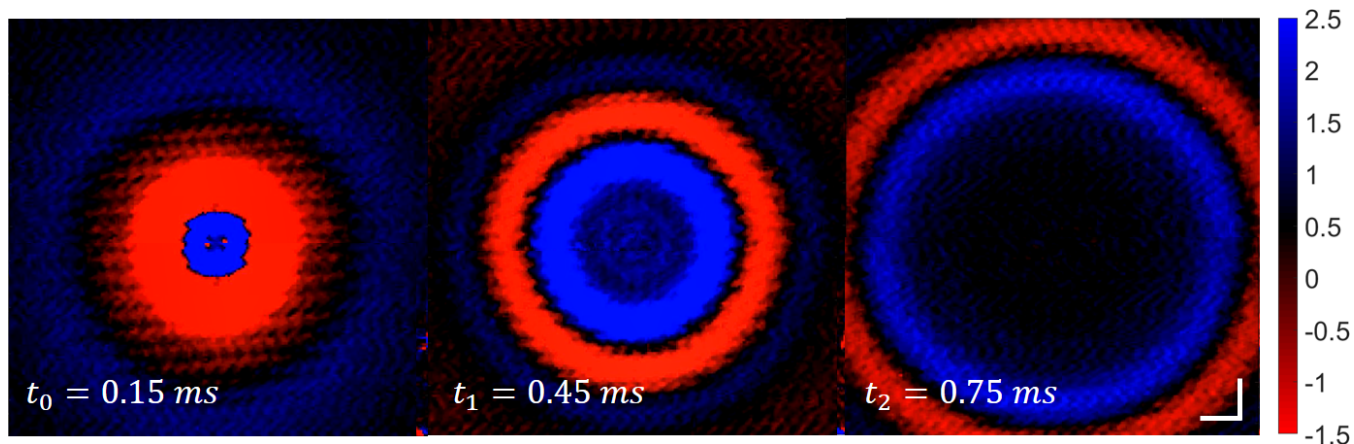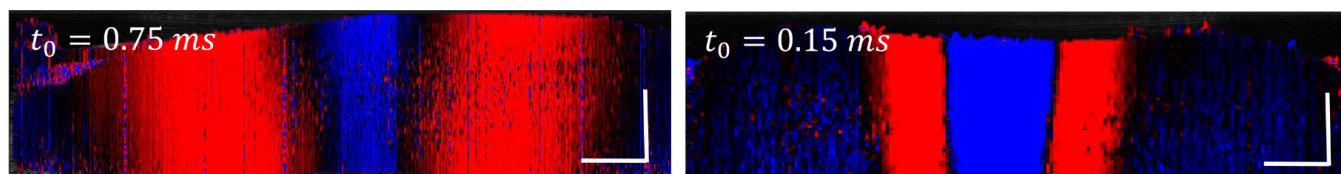

(a)

(b)

Fig. 6.   Wave propagation of a Gaussian-shaped pulse in phantoms. (a), (b) Snapshots of pulse propagation in the surface of the viscoelastic and elastic phantoms, respectively. Supplemental videos are available online. (c), (d) Motion snapshots of cylindrical wave propagation at different instants for both cases. Color bar scale is in radians related to the OCT Doppler phase-shift caused by particle motion in phantoms (Eq. (16)). (e) Cross-sectional motion profile (xz-plane) centered at the excitation epicenter in the viscoelastic (left) and elastic (right) phantom. Scale bar: 1 mm.

$t_0 = 0.75\ ms$ $t_1 = 1.05\ ms$ $t_2 = 1.35\ ms$

(c)

$t_0 = 0.15\ ms$ $t_1 = 0.45\ ms$ $t_2 = 0.75\ ms$

(d)

$t_0 = 0.75\ ms$ $t_0 = 0.15\ ms$

(e)

Fig. 6. (*Continued*)

the peak toward smaller values of frequency when r increases, which makes evident the presence of a frequency-dependent attenuation attributed to α_1. In contrast, this behavior is not strong for the elastic case as expected.

The Levenberg–Marquardt method was applied to Eq. (17) for different initial values of $\{c_0, c_1, \alpha_1\}$, and we found convergent solutions for the viscoelastic and elastic cases, as reported in Table 2. Equation (9) is mesh plotted in the $f - r$ space

using the optimized parameters $\{c_0^*, c_1^*, \alpha_1^*\}$ in Figs. 7(c) and 7(d) for the viscoelastic and elastic cases, respectively. We also included in Figs. 7(e) and 7(f), the profile plots extracted at four different r_0 positions from plots in Figs. 7(c) and 7(d), respectively, for a better comparison of the experimental data and model predictions.

Given the results of mechanical testing in Table 1, we plotted the real and imaginary parts of the wavenumber as a function of frequency using
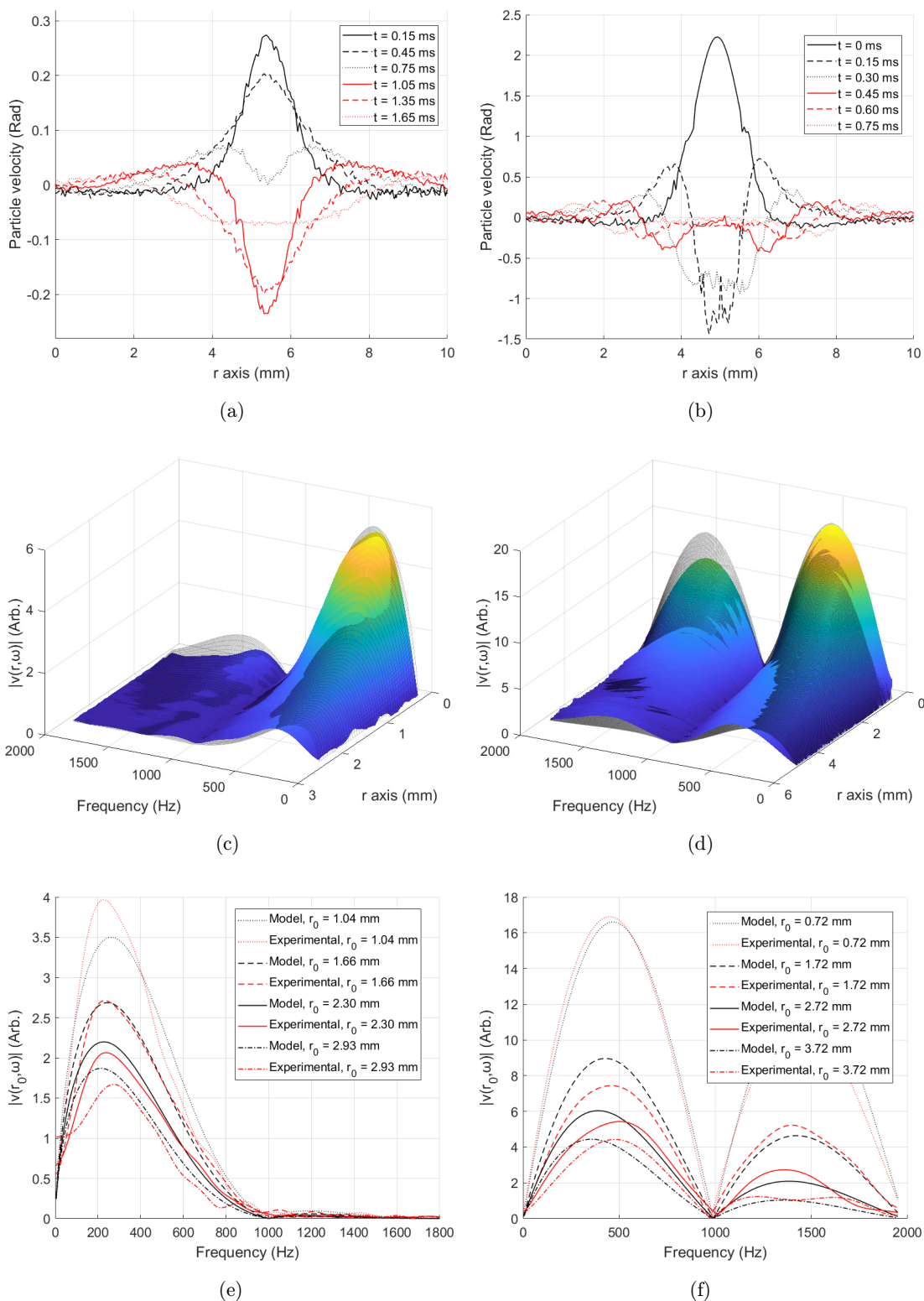
Fig. 7. Experimental plots of $v_{z_0}(x, y, t)$ (left col.), and $|\hat{v}_{z_0}(r, \omega)|$ (right col.) for a viscoelastic (a), (c) and elastic (b), (d) media. $\omega = 2\pi f$, and f = frequency. For all cases, the input force has an approximate Gaussian shape as described in Eq. (7), and $a = 1$ ms. Black mesh in (c), (d) shows $|\hat{v}(r, \omega)|$ for the optimized parameters $\{c_0^*, c_1^*, \alpha_1^*\}$ using the Levenberg–Marquardt inversion method. Profile plots extracted at four different r_0 positions in plots (c) and (d) are shown in (e) and (f), respectively for a better comparison of the experimental data and model prediction. Particle velocity units are shown in radians referring to OCT Doppler phase-shift and can be transformed to m/s using Eq. (16).

Table 2. Estimation of optimized parameters $\{c_0^*, c_1^*, \alpha_1^*\}$ using the Levenberg–Marquardt inversion method for solving Eq. (16) in experiments with phantoms and porcine cornea tissue.

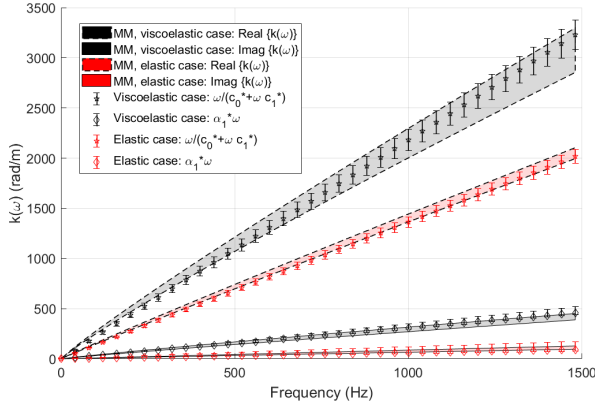|	c_0^* (m/s)	c_1^* (m/s/Hz)	α_1^* (NP/mm/kHz)
Viscoelastic phantom	2.88 ± 0.03	$9.75 \times 10^{-7} \pm 0.87 \times 10^{-7}$	0.049 ± 0.001
Elastic phantom	4.61 ± 0.02	$2.58 \times 10^{-7} \pm 0.14 \times 10^{-7}$	0.0098 ± 0.0005
Porcine cornea	2.11 ± 0.04	$2.42 \times 10^{-6} \pm 0.24 \times 10^{-6}$	0.055 ± 0.002

Fig. 8. Frequency-dependent wavenumber comparison between mechanical measurements (MM) results using the KVFD model and the application of our general propagation model (using optimized parameters $\{c_0^*, c_1^*, \alpha_1^*\}$). $\omega = 2\pi f$, and f = frequency. The real and imaginary parts of wavenumber is plotted as a function of frequency for the viscoelastic and elastic phantoms. Frequency-dependent results are the predictions of the KVFD model and our general propagation model, and they do not represent independent measurements over the frequency range.

Eq. (15) in Fig. 8, and we compared them with the components of the complex wavenumber obtained using results in Table 2 and Eq. (11). We found a good agreement of our model within the boundaries of the mechanical testing results for the viscoelastic and elastic cases. It is also evident that α_1^* for the viscoelastic case is half an order of magnitude higher compared to the elastic one, which was expected.

4.2. *Cornea experiment*

Figure 9 shows particle velocity frames $v_{z_0}(x, y; \{t_0, t_1, t_2\})$ for three different time instants extracted at the surface of a fresh porcine cornea. The ARF push location is found to be approximately at the center of the ROI. Figure 10(a) shows $v_{z_0}(r, t)$ obtained from a cropped profile cut in the x-direction centered to contain the ARF excitation origin. We compensated r values for the curvature of the cornea. After applying the Fourier transform, $|\hat{v}_{z_0}(r, \omega)|$ is shown in Fig. 10(b). A solution of
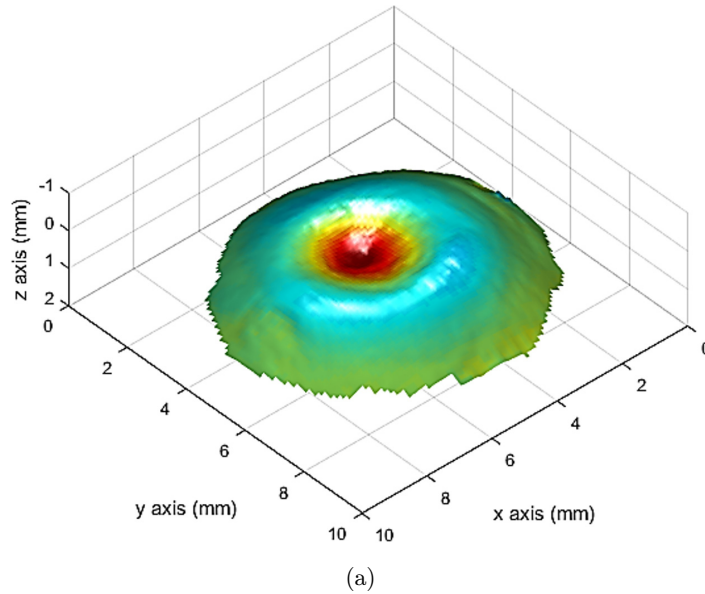

(a)

Fig. 9. Wave propagation of a Gaussian-shaped pulse in porcine cornea tissue. (a) Snapshot of pulse propagation in the surface of a fresh porcine cornea. Supplementary videos are provided online. (b) Particle velocity snapshots of wave propagation at different instants. Color bar scale is in radians related to the OCT Doppler phase-shift caused by particle motion in phantoms (Equation (16)).
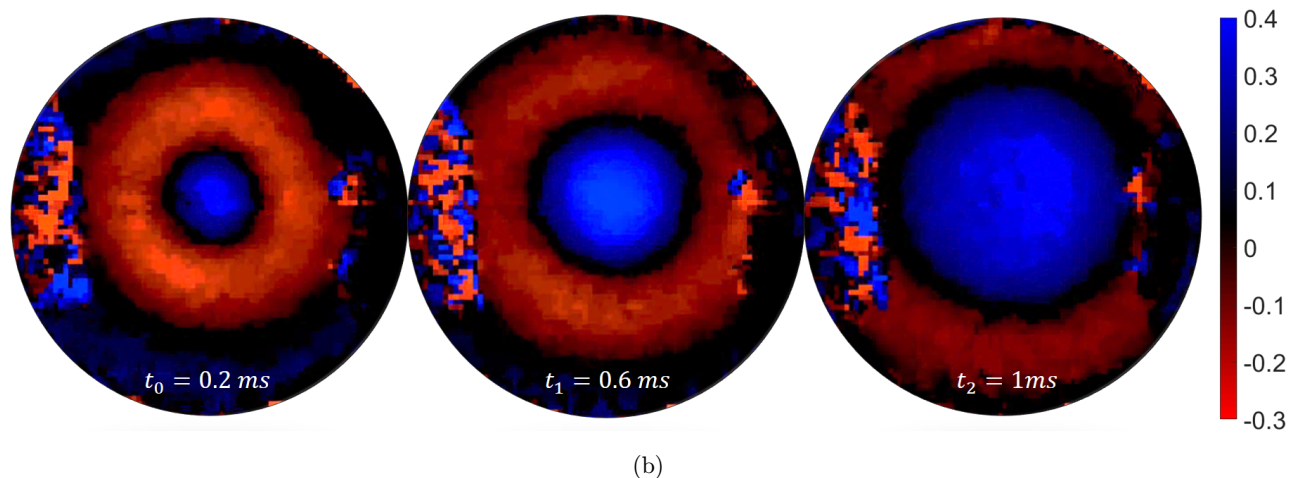
(b)

Fig. 9.   (*Continued*)
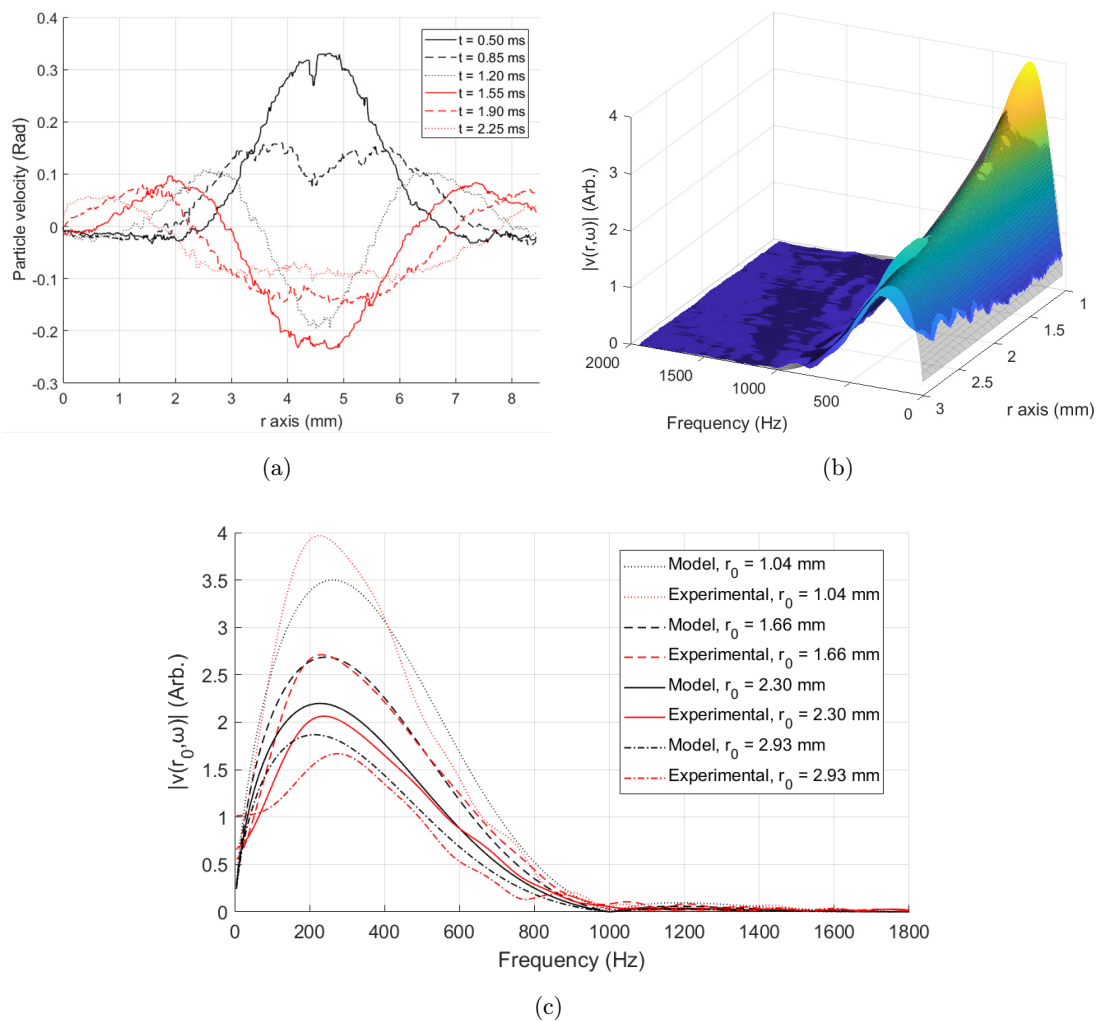

(a)

(b)

(c)

Fig. 10.   Experimental plots of $v_{z_0}(x, y, t)$ (a), and $|\hat{v}_{z_0}(r, \omega)|$ (b) for porcine corneal tissue. The input force has an approx. Gaussian shape as described in Eq. (7), and $a = 1$ ms. Black mesh in (b) shows $|\hat{v}(r, \omega)|$ for the optimized parameters $\{c_0^*, c_1^*, \alpha_1^*\}$ using the Levenberg–Marquardt inversion method. $\omega = 2\pi f$, and f = frequency. Profile plots extracted at four different r_0 positions in plots (b) are shown in (c), for a better comparison of the experimental data and model prediction. Particle velocity units are shown in radians referring to OCT Doppler phase-shift and can be transformed to m/s using Eq. (16).

Eq. (17) was obtained similarly as in the phantom cases in order to find $\{c_0^*, c_1^*, \alpha_1^*\}$. Optimized parameters are reported in Table 2.

Corneal phase speed c_0^* is found to be consistent with other studies developed in porcine cornea.[5,15] Attenuation parameter α_1^* trends similarly to the viscoelastic case when compared to phantom results, which plays an important role in the pulse distortion and damping during wave propagation as demonstrated in Fig. 10. For further viscous parameter comparison with other corneal studies, a rheological model needs to be carefully selected, which will be a matter of future work. In this study, we are not taking into consideration the specific boundary conditions of the cornea and, therefore, the presence of Lamb waves. Thus, speed results in the cornea reported here are solely valid for higher frequencies, when Lamb waves behave similarly to Rayleigh waves as described by Nenadic *et al.*[36] Concerning attenuation behavior, Lamb waves are spread and damped as described in Sec. 2 according to Schubert *et al.*[37] Therefore, attenuation results for corneal tissue shown in Table 2 are valid for the frequency-analyzed bandwidth.

Our current model is limited to the study of semi-infinite isotropic media which restricts its direct application to thin layers such as the cornea. However, this limitation can be resolved by extending the current general model for Lamb wave propagation in cylindrical coordinates and this will be the objective of future work. The acquisition time reported in this study is large and limits its application to *ex vivo* studies. The purpose of this research was to validate our method for the viscoelastic characterization of tissue. After validation, a faster and more stable OCT acquisition approach can be implemented for *in vivo* applications, as demonstrated by Singh *et al.*[38] and Song *et al.*[39] In addition, holographic techniques[40,41] demonstrated the fast acquisition of surface wave propagation in tissue, which offers an alternative to implement OCE methods in real time.

5. Conclusion

The application of an analytical general cylindrical wave propagation model for the viscoelastic characterization of dispersive media has been demonstrated. Experimental results in elastic and viscoelastic phantoms support the effectiveness of the approach when compared to mechanical testing results. Our proposed model of propagation takes into account (1) the initial force shape of the excitation pulse in the space-time field, (2) wave speed dispersion, (3) wave attenuation caused by material properties of the sample, (4) wave spreading caused by the outward cylindrical propagation of the wavefronts, and (5) the rheological-independent estimation of the dispersive medium. The model is versatile enough to be tuned with any type of input push-force produced by the desired excitation method. Moreover, in contrast to the majority of approaches that use only the frequency-dependent wave speed data for the calculation of viscoelastic parameters using a rheological model, our approach utilizes the wave attenuation data, which is fundamental for the accurate viscoelastic characterization of the sample without assuming any rheological model. This last advantage is significant for the study of tissue with unknown mechanical behavior. Finally, wave propagation in porcine cornea was analyzed and compensated for cylindrical spreading using this approach. Viscoelastic parameters of this tissue were calculated and reported. Future work will extend this research to a general Lamb wave model using different rheological models of tissue for the accurate estimation of viscous parameters in porcine and human cornea, and their relationship with ocular diseases and treatments.

Acknowledgments

References

1. K. J. Parker, M. M. Doyley, D. J. Rubens, "Imaging the elastic properties of tissue: The 20 year perspective," *Phys. Med. Biol.* **56**(1), R1 (2011).
2. C. Schmitt *et al.*, "Noninvasive vascular elastography: Toward a complementary characterization tool of atherosclerosis in carotid arteries," *Ultrasound Med. Biol.* **33**(12), 1841–1858 (2007).
3. J. A. Mulligan *et al.*, "Emerging approaches for high-resolution imaging of tissue biomechanics with optical coherence elastography," *IEEE J. Sel. Top. Quantum Electron.* **22**(3), 1–20 (2016).

4. W. Drexler *et al.*, "Optical coherence tomography today: Speed, contrast, and multimodality," *J. Biomed. Opt.* **19**(7), 071412–071412 (2014).

5. S. Wang, K. V. Larin, "Noncontact depth-resolved micro-scale optical coherence elastography of the cornea," *Biomed. Opt. Exp.* **5**(11), 3807–3821 (2014).

6. S. Wang, K. V. Larin, "Shear wave imaging optical coherence tomography (SWI-OCT) for ocular tissue biomechanics," *Opt. Lett.* **39**(1), 41–44 (2014).

7. C. Li *et al.*, "Determining elastic properties of skin by measuring surface waves from an impulse mechanical stimulus using phase-sensitive optical coherence tomography," *J. Roy. Soc. Interf.* **9**(70), 831–841 (2012).

8. K. M. Kennedy *et al.*, "Quantitative micro-elastography: Imaging of tissue elasticity using compression optical coherence elastography," *Sci. Rep.* **5** 15538-1–15538-12 (2015).

9. C. Li *et al.*, "Detection and characterisation of biopsy tissue using quantitative optical coherence elastography (OCE) in men with suspected prostate cancer," *Cancer Lett.* **357**(1), 121–128 (2015).

10. F. Zvietcovich *et al.*, "Comparative study of shear wave-based elastography techniques in optical coherence tomography," *J. Biomed. Opt.* **22**(3), 035010–035010 (2017).

11. K. V. Larin, D. D. Sampson, "Optical coherence elastography – OCT at work in tissue biomechanics [Invited]," *Biomed. Opt. Expr.* **8**(2), 1172–1202 (2017).

12. K. J. Parker, N. Baddour, "The Gaussian shear wave in a dispersive medium," *Ultrasound Med. Biol.* **40**(4), 675–684 (2014).

13. P. Garteiser *et al.*, "MR elastography of liver tumours: Value of viscoelastic properties for tumour characterisation," *Europ. Radiol.* **22**(10), 2169–2177 (2012).

14. K.-J. Streitberger *et al.*, "High-resolution mechanical imaging of glioblastoma by multifrequency magnetic resonance elastography," *PLOS ONE* **9**(10), e110588 (2014).

15. Z. Han *et al.*, "Quantifying tissue viscoelasticity using optical coherence elastography and the Rayleigh wave model," *J. Biomed. Opt.* **21**(9), 090504–090504 (2016).

16. X. Zhang, "Identification of the Rayleigh surface waves for estimation of viscoelasticity using the surface wave elastography technique," *J. Acoust. Soc. Am.* **140**(5), 3619–3622 (2016).

17. Z. Han *et al.*, "Optical coherence elastography assessment of corneal viscoelasticity with a modified Rayleigh-Lamb wave model," *J. Mech. Behav. Biomed. Mater.* **66**, 87–94 (2017).

18. P. Wijesinghe *et al.*, "Parametric imaging of visco-elasticity using optical coherence elastography," *Phys. Med. Biol.* **60**(6), 2293 (2015).

19. C. Schmitt, A. Hadj Henni, G. Cloutier, "Ultrasound dynamic micro-elastography applied to the viscoelastic characterization of soft tissues and arterial walls," *Ultrasound Med. Biol.* **36**(9), 1492–1503 (2010).

20. I. Z. Nenadic *et al.*, "Attenuation measuring ultrasound shearwave elastography and in vivo application in post-transplant liver patients," *Phys. Med. Biol.* **62**(2), 484 (2017).

21. S. Kazemirad *et al.*, "Ultrasound shear wave viscolastography: Model-independent quantification of the complex shear modulus," *IEEE Trans. Ultrason. Ferroelectr. Freq. Control* **63**(9), 1399–1408 (2016).

22. N. C. Rouze, M. L. Palmeri, K. R. Nightingale, "An analytic, Fourier domain description of shear wave propagation in a viscoelastic medium using asymmetric Gaussian sources," *J. Acoust. Soc. Am.* **138**(2), 1012–1022 (2015).

23. N. Leartprapun, R. Iyer, S. G. Adie, "Model-independent quantification of soft tissue visco-elasticity with dynamic optical coherence elastography," *Proc. Optical Coherence Tomography and Coherence Domain Optical Methods in Biomedicine* XXI, San Francisco, CA (2017).

24. K. F. Graff, *Wave Motion in Elastic Solids*, pp. 283–288. Dover Publications (2012).

25. N. Baddour, "Multidimensional wave field signal theory: Mathematical foundations," *AIP Adv.* **1**(2), 022120 (2011).

26. E. L. Carstensen, K. J. Parker, "Physical models of tissue in shear fields," *Ultrasound Med. Biol.* **40**(4), 655–674 (2014), This article is dedicated to our friend and colleague, Robert C. Waag.

27. D. T. Blackstock, *Fundamentals of Physical Acoustics*, Chap. 9, Wiley (2000).

28. F. Zvietcovich *et al.*, "Experimental classification of surface waves in optical coherence elastography," *Proc., Optical Elastography and Tissue Biomechanics III*, K. V. Larin, D. D. Sampson, Eds. San Francisco, CA (2016), doi: 10.1117/12.2211420.

29. I. A. Viktorov, *Rayleigh and Lamb Waves: Physical Theory and Applications*, Chap. 1, Springer US (2013).

30. M. Abramowitz, I. A. Stegun, *Handbook of Mathematical Functions: With Formulas, Graphs, and Mathematical Tables*, Dover Publications (2012).

31. M. Zhang *et al.*, "Quantitative characterization of viscoelastic properties of human prostate correlated with histology," *Ultrasound Med. Biol.* **34**(7), 1033–1042 (2008).

32. J. Yao *et al.*, "Angular scan optical coherence tomography imaging and metrology of spherical gradient refractive index preforms," *Opt. Exp.* **23**(5), 6428–6443 (2015).

33. P. Meemon, K. Lee, J. Rolland, "Doppler imaging with dual-detection full-range frequency domain optical coherence tomography," *Biomed. Opt. Expr.* **1**(2), 537–552 (2010).

34. T. Loupas, R. B. Peterson, R. W. Gill, "Experimental evaluation of velocity and power estimation for ultrasound blood flow imaging, by means of a two-dimensional autocorrelation approach," *IEEE Trans. Ultrason. Ferroelect. Freq. Control* **42**(4), 689–699 (1995).

35. J. J. Moré, "The Levenberg-Marquardt algorithm: Implementation and theory," *Proc. Biennial Conf. on Numerical Analysis*, Dundee, June 28–July 1, 1977, G. A. Watson, Ed., pp. 105–116, Springer, Berlin (1978).

36. I. Z. Nenadic *et al.*, "On Lamb and rayleigh wave convergence in viscoelastic tissues," *Phys. Med. Biol.* **56**(20), 6723–6738 (2011).

37. K. J. Schubert, A. S. Herrmann, "On attenuation and measurement of Lamb waves in viscoelastic composites," *Compos. Struct.* **94**(1), 177–185 (2011).

38. M. Singh *et al.*, "Phase-sensitive optical coherence elastography at 1.5 million A-Lines per second," *Opt. Lett.* **40**(11), 2588–2591 (2015).

39. S. Song *et al.*, "Strategies to improve phase-stability of ultrafast swept source optical coherence tomography for single shot imaging of transient mechanical waves at 16 kHz frame rate," *Appl. Phys. Lett.* **108**(19), 191104 (2016).

40. C. H. Liu *et al.*, "Non-contact single shot elastography using line field low coherence holography," *Biomed. Opt. Expr.* **7**(8), 3021–3031 (2016).

41. S. Li *et al.*, "Toward soft-tissue elastography using digital holography to monitor surface acoustic waves," *J. Biomed. Opt.* **16**(11), 116005 (2011).